INFLUENCE OF DESIGN PARAMETERS ON THE COMPRESSIVE STRENGTH OF 3D PRINTED SCAFFOLDS

Shreeprasad MANOHAR [1,2,*], Chinmoy DAS [3], Prof. Vikramjit KAKATI [1]

Lower limb injuries and bone tumors demand scaffolds with high compressive strength for structural stability. This study investigates biodegradable poly-L-lactic acid (PLLA) scaffolds fabricated via material extrusion, emphasizing the effect of infill pattern and density. Traditional designs (grid, line, triangular, tri-hexagon, zigzag, cross) and six novel patterns were evaluated. Ninety samples were tested under ASTM D695 standards, and results were validated using Finite Element Analysis. One-way ANOVA ($p < 0.05$) and Tukey's HSD confirmed significant differences. Triangle 50% infill achieved maximum compressive strength, while the novel Circular 58% design provided balanced strength and surface area, confirming suitability for lower limb applications.

Keywords: Biodegradable PLLA Scaffolds, Compressive Strength, infill patterns, ASTM D695 Compression Standards, Finite Element Analysis.

1. Introduction

Optimal bone health is fundamental in all life stages and contributes significantly to human development. Bones not only form the structural framework of the body but also provide protection to vital organs and house muscles and serve as calcium reservoirs. The intricate interplay between bones ensures internal organ safeguarding, enhances stability, and fosters synergy. Disruptions to this delicate balance, stemming from injuries, bacterial infections, or cancerous tissues, profoundly impact an individual's overall well-being. Human bones achieve peak density and maximal tissue development by 20 years of age, maintaining healthy proportions for approximately 35 years. Within the age range of 18–35 years, individuals are highly active but susceptible to accidents, constituting a significant portion of road accident victims in India [1]. Metal implants, commonly employed for post-accident injuries, often require two surgeries: an implantation procedure and a subsequent removal surgery, with suboptimal restoration of full functionality.[2]

* Corresponding author
[1] Ph.D. Scholar, Assam Don Bosco University, Guwahati, Assam
[2] Assistant Professor, Mechanical Department, The Bombay Salesian Society's Don Bosco Institute of Technology, Mumbai, India, email: smanohar@dbit.in
[3] Professor and HOD, Dept. of Orthopaedics, Tezpur Medical College & Hospital, Assam, India
[1] Professor, Mechanical Department, Assam Don Bosco University, Guwahati, Assam

Beyond trauma-related injuries, bone tumors pose a substantial concern. Osteosarcoma, a prevalent malignant bone tumor, predominantly affects children and constitutes a considerable proportion of childhood cancers in India [3]. Treatment typically involves excision or resection of the affected bony region, presenting challenges, especially in rural areas lacking advanced medical facilities [4].

The conventional bone grafting procedure, which necessitates the use of external bones from cadavers or patients, poses rejection risks and procedural challenges [5]. Tissue-engineered bone scaffolds have emerged as promising alternatives to mitigate rejection risks and provide a viable solution for complex infectious regions [6]. 3D printing technologies facilitate the creation of intricate bone scaffolds using biodegradable and biocompatible materials, such as PLA, PCL and PLGA, as well as composite blends such as PCL mixed with hydroxyapatite or simulated body fluid, which help improve the scaffold's strength and biological performance [7]. This technique allows the customization of scaffolds in terms of shape and size, offering additional cell sites for bone tissue growth. Notably, electrospun PLLA scaffolds with tunable surface potential and enhanced piezoelectricity significantly improve early osteoblast adhesion, making them promising candidates for bone regeneration [8]. However, successful implementation faces challenges related to vascularization, which is crucial for new bone generation [9]. Vascularization depends on the scaffold porosity, which influences the rate of blood cell growth [10]. Immunomodulatory strategies play a pivotal role in scaffold degradation, with the particle size affecting the inflammatory response [11]. A balance between infill density and immunomodulatory control is essential for optimal scaffold performance [12]. Adding reinforcement can improve the properties of polymer scaffolds. Research on zircon, $FeTiO_3$–SiO_2, and $ZrSiO_4$–TiO_2 reinforced epoxy composites shows that using dual nanoparticles at about 5:5 wt% gives the best improvement in strength, toughness, and wear resistance. This approach could also be useful in bone scaffold design to improve mechanical strength and biological performance [13] [14] [15]. Rutile (TiO_2) reinforced GFRP composites also show strong improvements, with 15 wt% providing the highest tensile and flexural strength, and intermediate levels enhancing hardness and impact strength. These studies demonstrate that optimized nanoparticle inclusion enhances composite strength and toughness, offering valuable strategies for bone scaffold design where mechanical reliability and bioactive surfaces are critical [16]. In addition, thermogravimetric studies show that dual-filler systems at 5:5 wt% also improve thermal stability, further supporting their potential for use in durable and reliable bone scaffold applications [17].

For lower-limb bone scaffolds, mechanical strength is imperative, particularly against compressive loads [18]. Compressive loads dominate the lower limbs, necessitating scaffolds that are both strong and porous, providing an ample surface area for tissue migration, proliferation, and vascularization [19].

Despite extensive experimental studies on the compressive strength of 3D-printed scaffolds, there remains a research gap in validating these findings through computational simulation. Moreover, limited attention has been given to scaffolds designed specifically for lower-limb bones, such as those in the foot. In the present study, poly-L-lactic acid (PLLA) is selected as the scaffold material due to its biodegradability, favorable mechanical properties, and compatibility with the Material Extrusion (MEX) additive manufacturing process. In addition to its technical merits, PLLA offers a cost-effective alternative to conventional implant materials, which is particularly relevant in the context of tumor resection procedures often associated with high treatment costs and limited accessibility in resource-constrained settings [20]. The goal is to test the scaffold's strength through both experimental compression testing and Finite Element Analysis (FEA), with a special focus on how well it works for rebuilding foot bones.

2. Material and methods

To prepare the sample, a biodegradable PLLA material is used which has following material properties given in Table 1.

Table 1

Material properties of PLLA

Properties	Values
Diameter of Filament	1.75 mm
Melting Point	175^{O} C
MFI (190°; 2.16 kg)	3 g/10min
Tensile strength at break	50 MPa
Density	1.24 g/cm^3
Young's Modulus	3500 MPa
Flexural Modulus	3350 MPa
Charpy impact strength (unnotched)	21 kJ/m^2

PLLA is a semicrystalline polymer and it showcases up to 37% crystallinity [21]. While printing, the printing temperature was kept at 200^{O} C. All the 90 test samples are printed using PLLA material. During the print, layer height was kept at 0.1 mm, print speed was kept at 70 mm/sec and all the samples were kept at center position on print bed [22]. They were printed individually one by one to maintain same printing conditions for all the samples [23].

In FDM, the infill pattern plays a pivotal role in determining the strength of 3D-printed scaffolds. The polymer filament was fed into the extruder, locally melted, and subsequently deposited layer-by-layer onto the heated glass bed. To systematically design and test bone scaffolds, the ASTM D695 standard was

employed, which specifies the specimen dimensions for polymer compression testing. Cylindrical specimens were adopted for this study because of the absence of corners, with dimensions set at a diameter of 12.7 mm and height of 25.4 mm refer to Figure 1 a). [24]

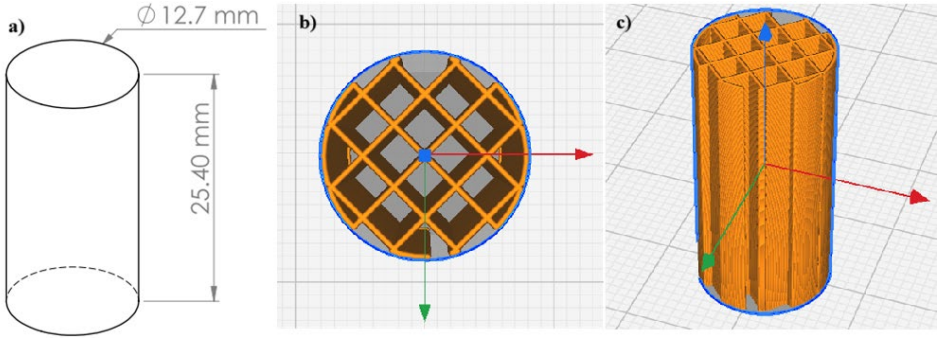

Fig. 1: a) ASTM D695 standard specimen dimensions b) 2D grid pattern top view and c) isometric view

In lower limb applications, where compressive strength is a critical design consideration, two-dimensional (2D) infill patterns are favored over three-dimensional (3D) configurations due to their superior load-bearing efficiency and structural reliability. The chosen 2D patterns grid, line, triangle, tri-hexagon, zigzag, and cross as shown in Figure 1 (b and c) maintain constant cross-sectional areas along all xy-planes throughout the z-axis, ensuring uniform strength during compressive loading. (Figure 1b and 1c are shown for reference to showcase how 2D patterns have same cross-section area in z-axis) [25]. Refer Figure 2 and Figure 3 for 2D patterns at 30% infill density and 50% infill density respectively for their cross-sectional dimensions. While 3D patterns exhibit varying cross-sections along the z-axis, rendering them weaker in load-bearing scenarios, all 3D patterns were excluded from this study to focus on optimizing the compressive strength [26].

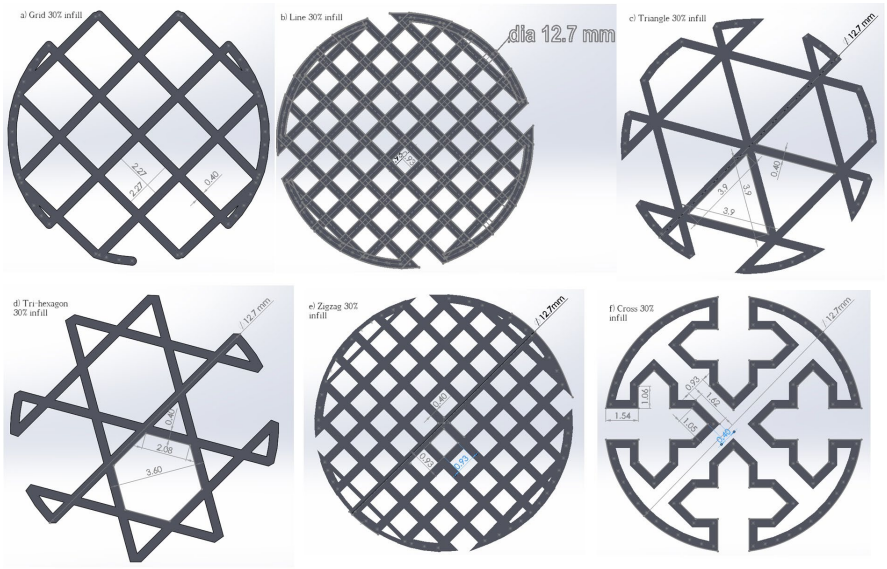

Fig. 2: Cross-sectional dimensions of 2D patterns at 30% infill densities

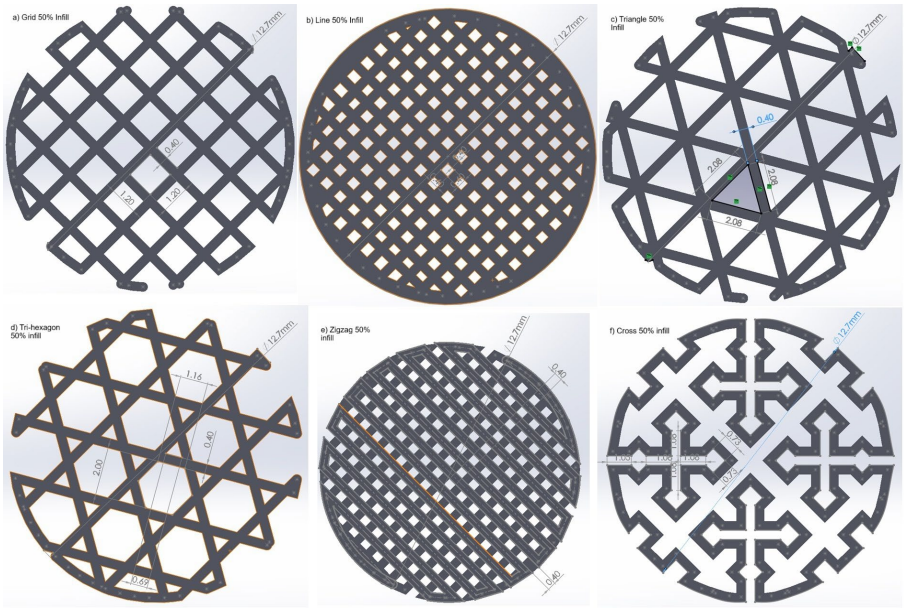

Fig. 3: Cross-sectional dimensions of 2D patterns at 50% infill densities

2.1 Infill Density and Pattern Selection

Infill density is a critical factor for bone scaffold functionality, varying from 0% (outer wall only) to 100% (fully filled). To balance sufficient compressive strength with the voids necessary for bone tissue growth, infill densities between 30% and 62% were selected. This range achieves optimal mechanical strength while providing ample surface area for cell growth, which is

vital for supporting lower-limb applications [27]. Moreover, as these scaffolds are designed for direct interaction with adjacent bone tissue, the samples are printed without outer walls or solid layers at the top and bottom surfaces. This open structure facilitates enhanced bone cell migration and proliferation.

Six fundamental 2D infill patterns (grid, line, triangle, tri-hexagon, zigzag, and cross) were studied at infill densities of both 30% and 50%. The study showcases an important benchmark, showing how topology optimization outcomes can be meaningfully compared with the practical behaviors of Fused Deposition Modeling based infill patterns, where anisotropy and process-specific characteristics influence the actual mechanical response [28]. Among these, the triangular and grid infill patterns were found to optimize impact energy absorption and compressive strength, respectively, in FDM 3D-printed PLA specimens [29]. Additionally, six novel 2D infill patterns have been proposed to enhance the surface area for bone tissue migration and proliferation, while maintaining scaffold strength. The newly suggested patterns include circular patterns with 58% and 62% infill, cross-concentric pattern (38% infill), curve concentric pattern (50% infill), and spiral concentric pattern (50% infill) (Figure 5). New infill patterns have been specifically designed based on the concept of curvature to address limitations found in traditional 2D infill geometries. Refer Figure 6 for the cross-sectional dimensions of newly designed patterns. Conventional 3D printing infill patterns are fundamentally based on straight lines and linear intersections. While these straight-line patterns offer mechanical stability, they do not fully replicate the complex, curved architecture of natural bone, especially in load-bearing regions like the lower limbs. Natural bone tissue, particularly trabecular bone, exhibits a highly porous and curved microstructure, which plays a crucial role in distributing loads efficiently and facilitating the migration of bone cells. By introducing curvature-based infill patterns, the aim is to more closely mimic this biological architecture. These curved patterns enhance internal surface area and create a more biomimetic environment that encourages better cell attachment, proliferation, and nutrient flow.

Furthermore, curvature-based designs help in evenly distributing mechanical stresses, reducing stress concentrations that typically occur at sharp angles in traditional patterns. As a result, these new infill geometries are expected to provide not only improved biological performance but also better mechanical resilience under compressive loads making them especially suitable for bone scaffolds intended for lower limb support.

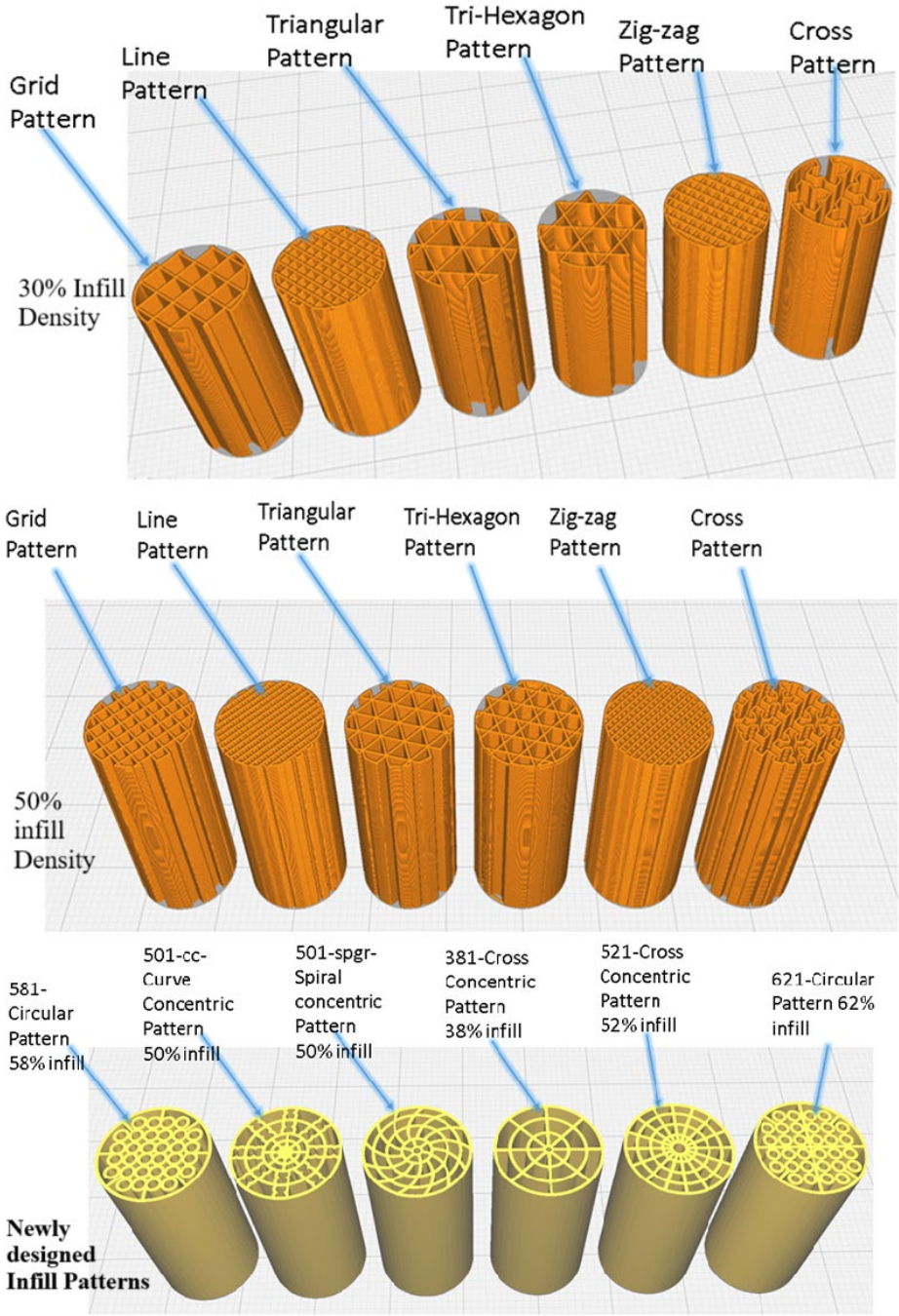

Fig. 5: Basic 2D infill patterns with 30% infill densities (on top), 50% infill densities (at center) and newly proposed infill patterns (at bottom)

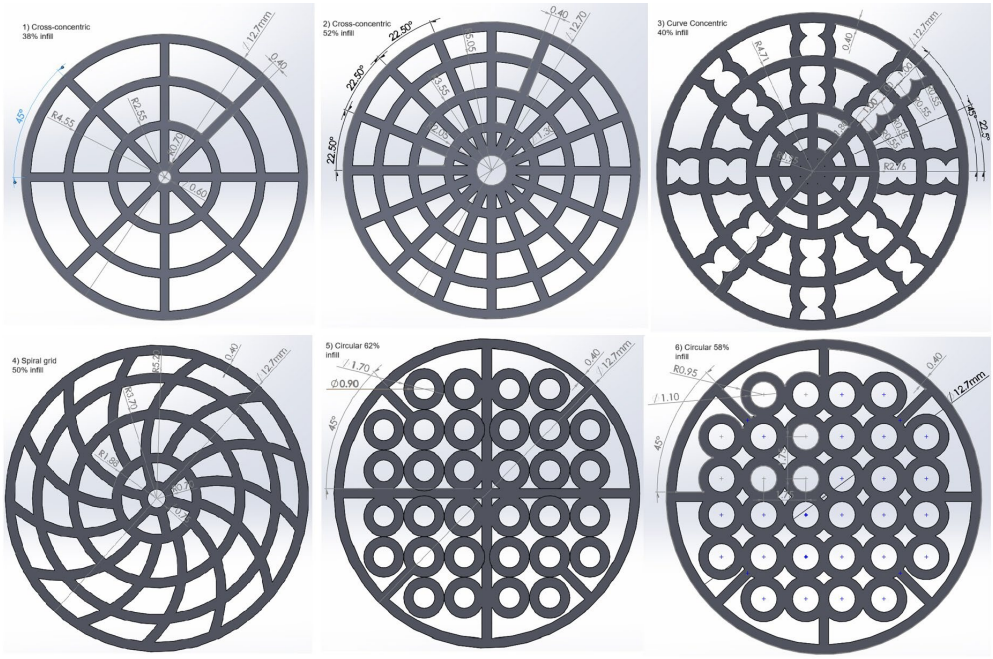

Fig. 6: Cross-sectional dimensions of newly designed infill patterns

2.2 Compression Testing of Samples

In accordance with ASTM D695 standards, a rigorous compression testing protocol was implemented for each combination of infill pattern and infill density, involving 3D printing and testing of five distinct samples. The purpose was to evaluate the compressive strength of the bone scaffolds using a Fine group's standard universal testing machine (TUE-CN-1000), maintaining a constant strain rate of 1.3 mm/min throughout all tests [30]. To simulate real-world loading conditions, the samples were positioned precisely at the center between two flat plates, and the tests were conducted until permanent deformation was observed, surpassing the elasticity limit.

The resulting load versus deformation graphs were generated for each test, offering insights into the behavior of the scaffold under compressive loading. A series of compression tests were conducted on 90 samples to evaluate their mechanical response under increasing load. The recorded data for one representative sample of tri-hexagon pattern at 30% infill shows a progressive rise in compressive force from approximately 81 N at 0.017 mm deformation to 2579.86 N at 1.055 mm deformation. Subsequently, plastic strain versus true stress graphs were derived from the collected data to provide a comprehensive understanding of the mechanical response of the scaffold. The compression testing outcomes are visually depicted in Figure 7, which show distinct responses for various infill patterns and densities.

Fig. 7: Compression testing of all samples as per ASTM D695 standard

As a representative reference, Figure 8 shows a sample graph of true stress versus plastic strain for the triangle pattern with 50% infill density. The values on top of each point represent the applied compressive force in Newtons. This example helps illustrate how each infill pattern and density was analyzed to understand the scaffold's mechanical behavior.

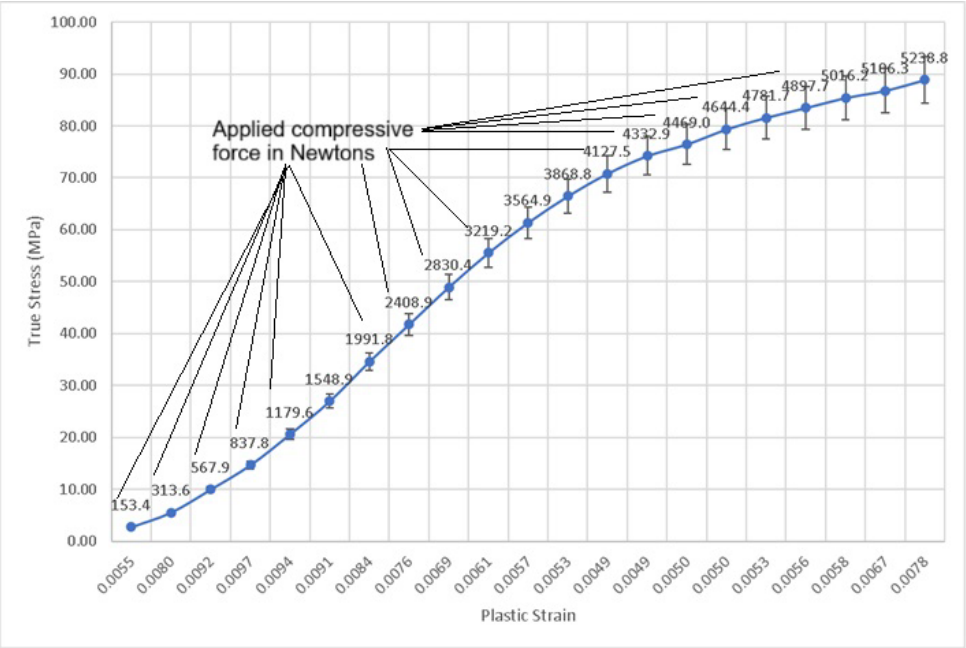

Fig. 8: Graph of Experimental Results of True Stress v/s Plastic Strain for a 503- triangle pattern - 50% Infill Density (graph by the author)

A compilation of the compression test setup can be seen in Table 2. All the below experiments were performed 5 times to ensure repeatability of the experiment encompassing 90 compression tests. The table details each sample and specifies the infill pattern, infill density, and corresponding identification numbers.

Table 2: Compression test setup for infill pattern and infill density combination

Sr. No.	Sample Name	Infill Pattern	Infill Density (%)
1	301	Grid-30	30
	501	Grid-50	50
2	302	Line-30	30
	502	Line-50	50
3	303	Triangle-30	30
	503	Triangle-50	50
4	304	Trihexagon-30	30
	504	Trihexagon-50	50
5	305	Zigzag-30	30
	505	Zigzag-50	50
6	306	Cross-30	30
	506	Cross-50	50

7	581	Circular-58	58
	621	Circular-62	62
8	381	Cross-concentric-38	38
	521	Cross-concentric-52	52
9	501-CC	Curve-concentric	50
10	501-SpGr	Spiral concentric	50

2.3 Simulation Setup

Using true stress versus plastic strain data from five samples for each infill pattern and density, Young's modulus was calculated to define the material properties of the polymer under study. These properties were then used to create detailed material input data for simulation in ANSYS Workbench's static structural module, where compression tests were virtually replicated.

To simulate the material's behavior under compressive loading, a multilinear hardening model was applied. This model, ideal for polymers, represents the nonlinear stress-strain response using a series of linear segments from the yield point to the ultimate strength. While it effectively models the material's plastic behavior, it does not account for the post-ultimate failure phase, where the stress-strain curve begins to decline.

In the nonlinear simulation setup, auto time stepping was used to apply the load incrementally, with 100 initial sub-steps and a maximum of 1000 to ensure solution accuracy. Additionally, the large deflections setting was enabled to account for significant deformations, which commonly occur in compression beyond the elastic limit, providing a more realistic simulation of the material's response.

The original model was transformed into a 3D axis-symmetric model by incorporating three symmetric planes: the xy, yz, and xz symmetry planes. This conversion aimed to streamline the model by reducing the number of elements, which is crucial for nonlinear analyses, as shown in Figure 9 (a to d). Figure 9 (a) showing the full 3D model of the scaffold. This model is then simplified into an axisymmetric representation to reduce computational complexity while preserving the accuracy of the analysis as seen in Figure 9 (b). The axisymmetric model is meshed with appropriate element sizing to capture stress variations accurately as seen in Figure 9 (c and d), followed by the application of boundary conditions simulating uniaxial compression i.e. fixed support at the base and compressive load applied from the top as seen in Figure 9 (e).

This triangle scaffold serves as the reference model for the finite element analysis (FEA) process. All remaining 17 scaffold samples, featuring different infill patterns and densities, were analyzed using the same modeling procedure. This consistent method made it possible to compare the simulation results

accurately and helped gather useful information about the mechanical performance of each scaffold design.

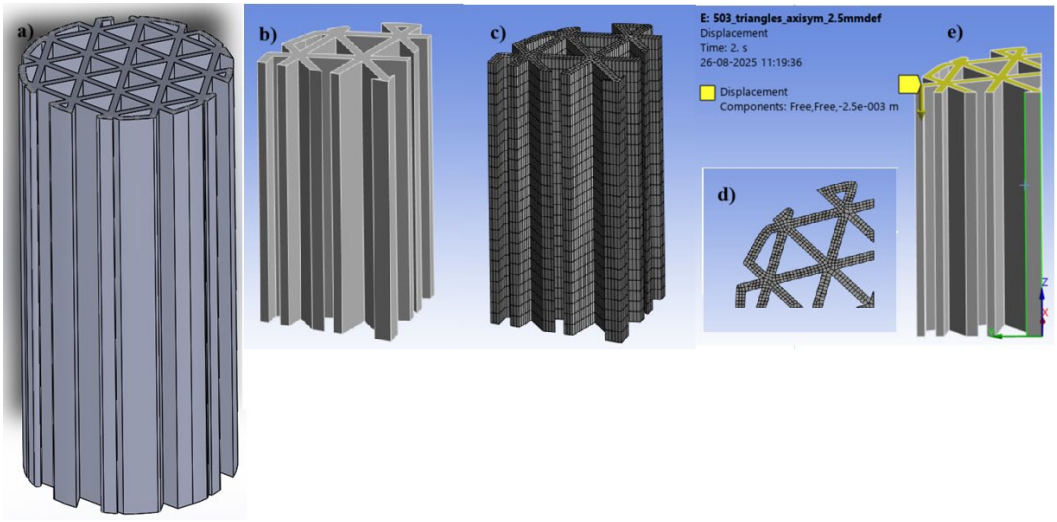

Fig. 9: a) Complete solid model of triangle infill pattern with 50% infill density, b) 3D axis-symmetric model c) Meshed model d) Ensured 4 elements across the wall thickness of the model e) Displacement boundary condition along the z-axis direction

All models were meshed with SOLID186 elements, which are higher-order 3D elements that exhibit quadratic displacement behavior. Each element comprises of 20 nodes, offering three degrees of freedom (DOF) per node. The total mesh count was 15407 with 78732 number of nodes. The mesh count was controlled due to axisymmetric modeling which helped to reduce mesh count from 61628 to 15407. The wall thickness was 0.4mm and it was kept constant for all the 18 samples which were analyzed. Based on the compression test results, the total deformation value was applied as a displacement boundary condition along the z-axis, as depicted in Figure 9(e). A nonlinear analysis employing a full Newton-Raphson procedure was established for each simulation.

3. Results and Discussions

Each simulation was conducted using a nonlinear analysis with a full Newton-Raphson procedure. The resulting graph compares the compressive strength obtained from experimental compression tests with the strengths predicted by the simulations, as detailed in Figure 10.

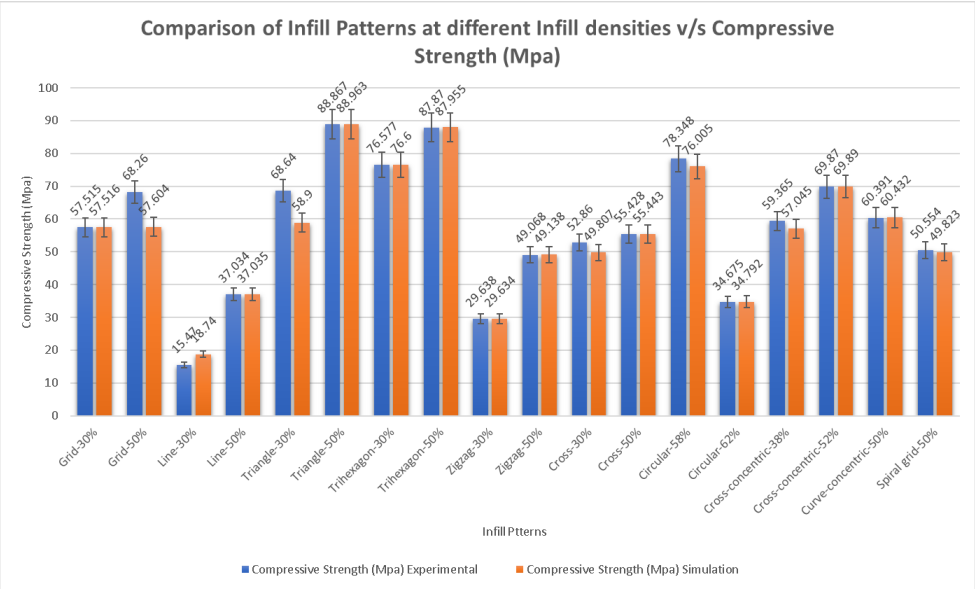

Fig. 10: Comparison of compressive strength obtained by experimental results v/s simulation results for 18 infill patterns and infill density combination

A detailed assessment of 3D-printed bone scaffolds was conducted to evaluate the impact of infill pattern and density on compressive strength, available surface area, and strength-to-weight ratio. Both experimental testing and finite element simulations (FEM) were performed to validate mechanical performance and ensure computational reliability. The results demonstrated that scaffold strength is highly dependent on both infill geometry and density. At 30% infill, the tri-hexagon pattern exhibited the highest compressive strength (76.577 MPa experimental; 76.6 MPa simulated, 0.03% error), confirming its robustness even with reduced material usage. The triangle pattern also showed good performance (68.64 MPa experimental; 58.9 MPa simulated) but with a larger deviation between experiment and simulation (14.17%), suggesting a limitation in the FEM model for this configuration at lower density. In contrast, the line pattern was mechanically unsuitable, with very low strength (15.47 MPa experimental; 18.74 MPa simulated, 21.07% overestimation). At higher densities, performance improved markedly. The triangle pattern at 50% infill demonstrated the highest compressive strength (88.867 MPa experimental; 88.963 MPa simulated), with an exceptionally low error (0.108%), validating the predictive accuracy of the FEM model. The tri-hexagon pattern at the same density also showed strong results (87.87 MPa experimental; 87.955 MPa simulated, 0.096% error). Other competitive performers included the cross-concentric pattern at 52% infill (69.87 MPa experimental; 69.69 MPa simulated, 0.028% error).

Statistical analysis mentioned in Table 3 confirms these findings. One-way ANOVA revealed a significant effect of infill configuration on compressive

stress, $F(17, 72) = 491.35$, $p < 0.001$, with a large effect size ($\eta^2 = 0.99$), indicating that nearly all variance was explained by pattern and density. Tukey's HSD test confirmed that the triangle pattern at 50% density (Group 503) produced the highest mean compressive strength (88.88 MPa, 95% CI: 88.59–89.17), significantly outperforming all other groups. Groups 504 (87.68 MPa), 581 (78.75 MPa), and 304 (76.98 MPa) also formed a high-strength cluster. By contrast, Groups 305 (29.24 MPa) and 302 (15.08 MPa) had the weakest performance.

Table 3: One-way ANOVA for compressive stress (MPa)

Source	**SS**	**df**	**MS**	**F**	**p-value**	**F crit**
Between groups	33679.77	17	1981.163	491.3539	< 0.001	1.7665
Within groups	290.3075	72	4.03209			
Total	33970.07	89				

Overall, the findings confirm that optimal scaffold strength is achieved with triangular and tri-hexagon geometries at higher infill densities, while simple line infill patterns are unsuitable for structural bone applications. In addition, the newly designed high–surface-area patterns (e.g., cross-concentric and curve-concentric variants) demonstrated promising results by balancing compressive strength with enhanced available surface area.

Figure 11 shows the simulation results for the triangle and tri-hexagon pattern with 50% infill density, showing the normal stress along the z-axis and total plastic strain along the z-axis. The red zone showcases weaker sections and scaffold failed at similar locations during the test. The results align with the experimental limits, demonstrating the effectiveness of the modeling approach.

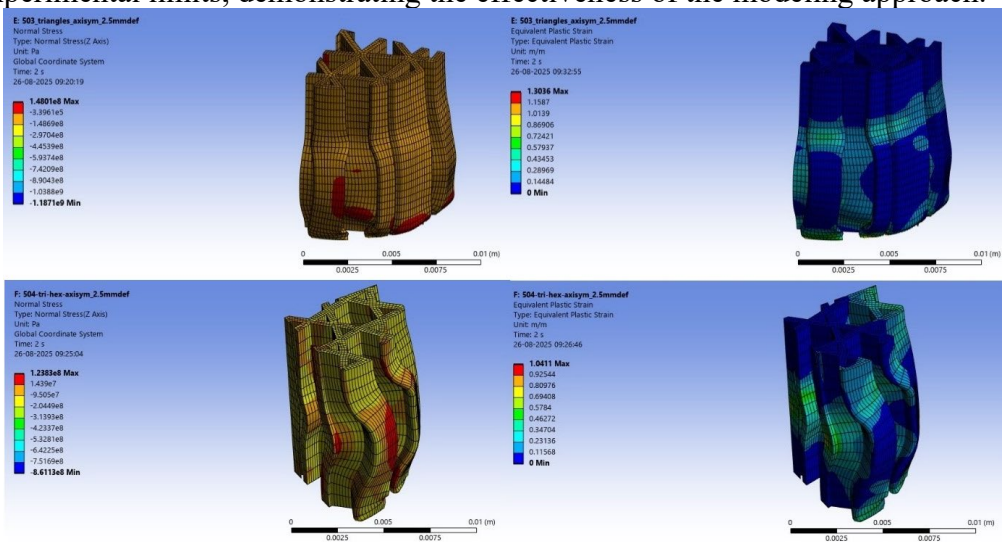

Fig. 11: Normal stress along z-axis (on the left) and total plastic strain along z-axis (on the right)

The simulation results matched very closely with experimental values for most patterns and densities, showing that the Finite Element Method (FEM) is a reliable tool for predicting scaffold performance. For example, the Tri-hexagon at 30% density showed only 0.03% error, Triangle at 50% had 0.108% error, Circular at 62% had 0.34% error, Zigzag at 30% had 0.013% error, and Cross at 50% had 0.027% error. The biggest difference was seen in the Grid pattern at 50%, where the simulation (57.604 MPa) was lower than the experimental strength (68.26 MPa) by about 15.6%. Overall, except for Grid-30%, Line-30%, and Triangle-30%, the average simulation error across all 18 patterns stayed below 5%, proving that the models are reliable for screening scaffold designs before physical testing.

Building on prior findings that higher mass directly enhances compressive strength, the selected intermediate density values (38%, 52%, 58%, and 62%) for the newly developed curvature-based infill patterns (cross-concentric and circular) ensured an optimal balance between structural integrity and weight for load-bearing scaffold applications [31]. These intermediate density values are supported by literature, which reports that PLA samples printed at 75% infill density showed the best overall performance [32]. Unlike conventional 2D line-based infills, these curved geometries generate substantially greater surface area as density increases. This characteristic is particularly valuable in tissue engineering, where higher surface area provides more potential sites for cell attachment and subsequent bone tissue growth [33]. For example, the circular pattern at 58% density achieved a surface area of 9493.55 mm^2 significantly higher than standard 50% density designs. Similarly, the cross-concentric pattern at 52% density produced 7295.59 mm^2, while the curve-concentric at 50% density reached 7105.64 mm^2. These values exceed the average surface areas of conventional infills, which were 5352.47 mm^2 at 30% density and 6681.79 mm^2 at 50% density. Figure 12 illustrates the percentage increase in surface area offered by these new designs compared with traditional patterns. The importance of curvature based patterns is well supported by literature where researchers have shown considerable bone growth in curvature based patterns i.e. gyroid pattern, diamond pattern compared with 2D line-based patterns through in vitro and in vivo tests [34][35]. Studies also showcase that TPMS gyroid architectures promote superior osseointegration by combining high surface area with biomimetic porous channels that facilitate bone ingrowth and vascularization [36]. The underlying advantage of curved patterns lies in their continuous arcs and smooth transitions, which naturally extend surface length and perimeter per unit volume, outperforming straight-line infills at equivalent densities.

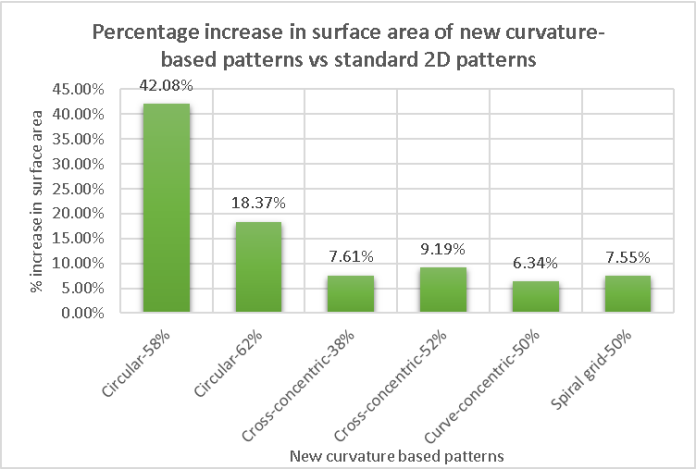

Fig. 12: Percentage increase in surface area of new curvature-based patterns vs standard 2D patterns

The strength-to-weight ratio (α) is a critical parameter for evaluating the efficiency of a scaffold material in load-bearing biomedical applications. A higher α indicates better mechanical performance with less material, ideal for patient-specific implant design refer to Figure 13 for strength-to-weight ratio of all infill patterns. At 50% infill, the triangle pattern exhibited the highest α value of 2619.41, coinciding with the maximum compressive strength (88.867 MPa). This makes it the most efficient structural pattern in the study.

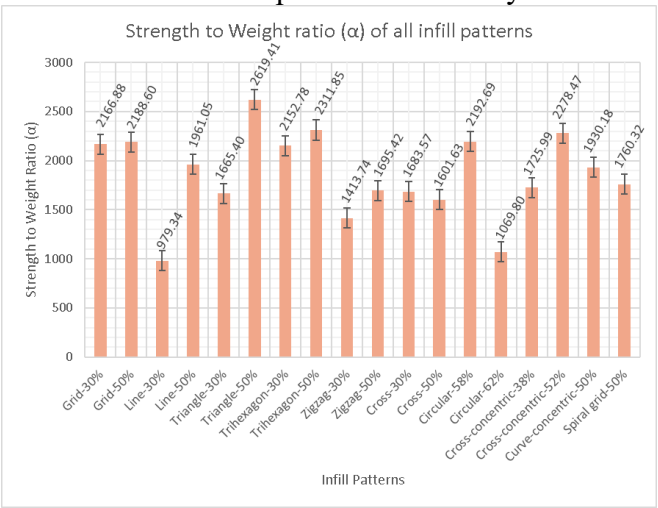

Fig. 13: strength-to-weight ratio of all infill patterns

The tri-hexagon-50% had a slightly lower α (2311.85) but comparable strength (87.87 MPa), showing its advantage in applications requiring geometric complexity and isotropy. Conversely, the line-30% pattern recorded the lowest α value of 979.34, coupled with the lowest strength, indicating very poor mechanical efficiency. The circular-58% pattern, despite its higher density,

maintained a strong α of 2192.69, showing excellent performance in strength while maximizing surface area for tissue interaction. The Table - 4 below summarizes all the results in a nutshell.

Table 4: Comparison of Strength to weight ratio (α), Available surface area, Compressive Strength (MPa) and % Error for each infill pattern and density combination

Sr. No.	Infill Pattern	Strength to weight ratio (α)	Available Surface Area (mm^2)	Compressive Strength (MPa)		% Error
				Experimental	Simulation	
1	Grid-30%	2166.88	4583.27	57.515	57.516	0.002
2	Grid-50%	2188.60	6175.13	68.26	57.604	-15.611
3	Line-30%	979.34	7023.97	15.47	18.74	21.138
4	Line-50%	1961.05	7844.07	37.034	37.035	0.003
5	Triangle-30%	1665.40	4660.82	68.64	58.9	-14.190
6	Triangle-50%	2619.41	6296.31	88.867	88.963	0.108
7	Trihexagon-30%	2152.78	3791.24	76.577	76.6	0.030
8	Trihexagon-50%	2311.85	5406.43	87.87	87.955	0.097
9	Zigzag-30%	1413.74	7260.04	29.638	29.634	-0.013
10	Zigzag-50%	1695.42	7880.95	49.068	49.138	0.143
11	Cross-30%	1683.57	4795.50	52.86	49.807	-5.776
12	Cross-50%	1601.63	6487.90	55.428	55.443	0.027
13	Circular-58%	2192.69	9493.55	78.348	76.005	-2.991
14	Circular-62%	1069.80	7909.45	34.675	34.792	0.337
15	Cross-concentric-38%	1725.99	5759.59	59.365	57.045	-3.908
16	Cross-concentric-52%	2278.47	7295.59	69.87	69.89	0.029
17	Curve-concentric-50%	1930.18	7105.64	60.391	60.432	0.068
18	Spiral grid-50%	1760.32	7185.97	50.554	49.823	-1.446

4. Conclusions

The comprehensive evaluation of 3D-printed bone scaffold infill patterns across varying densities revealed that both geometry and material distribution critically influence mechanical performance and biological potential. Infill density strongly affects compressive strength, with an effective range identified between 50–62%, while only select geometries at 30% achieved acceptable performance. This range supports both structural strength and biological functionality by allowing optimal void spaces for cellular activity, while the increased surface area

provides more sites for tissue growth. The ANOVA results confirmed statistically significant differences among the tested infill patterns ($p < 0.05$), with Tukey's post-hoc test highlighting the triangle infill pattern at 50% density as the most efficient design, demonstrating the highest compressive strength (88.867 MPa) and maximum strength-to-weight ratio ($\alpha = 2619.41$), making it ideal for load-bearing orthopedic applications. The tri-hexagon pattern also showed robust performance at both 30% and 50% infill densities, particularly excelling at lower densities with minimal simulation error, highlighting its suitability where material conservation is essential. The circular pattern at 58% infill offered an optimal balance of mechanical strength (78.348 MPa) and maximum surface area (9493.55 mm^2), making it a strong candidate for scaffold design. The simulation results showed high consistency with experimental data, confirming the validity of Finite Element Method as a reliable predictive tool in scaffold design optimization. These findings underscore the importance of strategic infill pattern selection in achieving tailored mechanical and biological outcomes, paving the way for the development of patient-specific, performance-optimized bone scaffolds.

Acknowledgments

The authors would like to acknowledge Assam Don Bosco University, School of Mechanical Engineering for their guidance and approval to carry out this research and The Bombay Salesian Society's Don Bosco Institute of Technology Mumbai for their continuous support towards this research

REFERENCES

[1] "Road accidents in India road accidents 2021. [Online]. Available: www.morth.nic.in

[2] *S. K. Singh*, "Road Traffic Accidents in India: Issues and Challenges," in Transportation Research Procedia, Elsevier B.V., 2017, pp. 4708–4719. doi: 10.1016/j.trpro.2017.05.484.

[3] *M. L. Wang, N. Y. Xu, R. Z. Tang, and X. Q. Liu*, "A 3D-printed scaffold-based osteosarcoma model allows to investigate tumor phenotypes and pathogenesis in an in vitro bone-mimicking niche," Mater Today Bio, vol. 15, Jun. 2022, doi: 10.1016/j.mtbio.2022.100295.

[4] *S. J. Taran, R. Taran, and N. B. Malipatil*, "Pediatric Osteosarcoma: An Updated Review," Indian Journal of Medical and Paediatric Oncology, vol. 38, no. 01, pp. 33–43, Jan. 2017, doi: 10.4103/0971-5851.203513.

[5] *S. Zhao et al.,* "Standardizing compression testing for measuring the stiffness of human bone," Bone Joint Res, vol. 7, no. 8, pp. 524–538, Aug. 2018, doi: 10.1302/2046-3758.78.BJR-2018-0025.R1.

[6] *E. Ryan and S. Yin*, "Compressive strength of β-TCP scaffolds fabricated via lithography-based manufacturing for bone tissue engineering," Ceram Int, vol. 48, no. 11, pp. 15516–15524, Jun. 2022, doi: 10.1016/j.ceramint.2022.02.085.

[7] *K. V. Niaza, F. S. Senatov, S. D. Kaloshkin, A. V. Maksimkin, and D. I. Chukov*, "3D-printed scaffolds based on PLA/HA nanocomposites for trabecular bone reconstruction," in Journal of Physics: Conference Series, Institute of Physics Publishing, Sep. 2016. doi: 10.1088/1742-6596/741/1/012068.

[8] *M. Polak, K. Berniak, P. K. Szewczyk, J. E. Karbowniczek, M. M. Marzec, and U. Stachewicz*, "PLLA scaffolds with controlled surface potential and piezoelectricity for enhancing cell adhesion in tissue engineering," Appl Surf Sci, vol. 621, p. 156835, Jun. 2023, doi: 10.1016/j.apsusc.2023.156835.

[9] *H. Yijun, L. Lin, L. Cheng, Z. Zhi Yong, and H. Jiongfeng*, "Strategies for in situ tissue engineering of vascularized bone regeneration (Review)," Biomed Rep, vol. 18, no. 6, 2023, doi: 10.3892/br.2023.1625.

[10] *D. S. Sparks, F. M. Savi, S. Saifzadeh, M. A. Schuetz, M. Wagels, and D. W. Hutmacher*, "Convergence of Scaffold-Guided Bone Reconstruction and Surgical Vascularization Strategies—A Quest for Regenerative Matching Axial Vascularization," Front Bioeng Biotechnol, vol. 7, Jan. 2020, doi: 10.3389/fbioe.2019.00448.

[11] *T. Zhao, Z. Chu, J. Ma, and L. Ouyang*, "Immunomodulation Effect of Biomaterials on Bone Formation," Sep. 01, 2022, MDPI. doi: 10.3390/jfb13030103.

[12] *C. Dong, G. Tan, G. Zhang, W. Lin, and G. Wang*, "The function of immunomodulation and biomaterials for scaffold in the process of bone defect repair: A review," 2023, Frontiers Media S.A. doi: 10.3389/fbioe.2023.1133995.

[13] *K. P. S. Perumal, R. Boopathi, L. Selvarajan, and K. Venkataramanan*, "The effects of zircon particles on the mechanical and morphological properties of glass fibre reinforced epoxy composite," Mater Today Commun, vol. 37, p. 107067, Dec. 2023, doi: 10.1016/j.mtcomm.2023.107067.

[14] *K. P. Srinivasa Perumal, L. Selvarajan, K. P. Manikandan, and C. Velmurugan,* "Mechanical, tribological, and surface morphological studies on the effects of hybrid ilmenite and silicon dioxide fillers on glass fibre reinforced epoxy composites," J Mech Behav Biomed Mater, vol. 146, p. 106095, Oct. 2023, doi: 10.1016/j.jmbbm.2023.106095.

[15] *K. P. Srinivasa Perumal, R. Boopathi, P. Saravanan, and L. Selvarajan*, "Effect of zircon and anatase titanium dioxide nanoparticles on glass fibre reinforced epoxy with mechanical and morphological studies," Ceram Int, vol. 49, no. 13, pp. 21667–21677, Jul. 2023, doi: 10.1016/j.ceramint.2023.03.304.

[16] *K. P. Srinivasa Perumal, L. Selvarajan, P. Mathan Kumar, and S. Shriguppikar*, "Enhancing mechanical and morphological properties of glass fiber reinforced epoxy polymer composites through rutile nanoparticle incorporation," Progress in Additive Manufacturing, vol. 10, no. 1, pp. 831–848, Jan. 2025, doi: 10.1007/s40964-024-00675-0.

[17] *K. P. Srinivasa Perumal, L. Selvarajan, S. M. Sekar, and E. Natarajan*, "Examining thermogravimetric response and morphological alterations in epoxy composites with hybrid ceramic fillers integration," Mater Chem Phys, vol. 325, p. 129755, Oct. 2024, doi: 10.1016/j.matchemphys.2024.129755.

[18] *E. Oksztulska-Kolanek, B. Znorko, M. Michałowska, and K. Pawlak*, "The biomechanical testing for the assessment of bone quality in an experimental model of chronic kidney disease," Nephron, vol. 132, no. 1, pp. 51–58, 2016, doi: 10.1159/000442714.

[19] *D. Kong, Y. Shi, G. Lin, B. Jiang, and J. Du*, "Recent Advance in Evaluation Methods for Characterizing Mechanical Properties of Bone," Archives of Computational Methods in Engineering, vol. 27, no. 3, pp. 711–723, Jul. 2020, doi: 10.1007/s11831-019-09322-2.

[20] *S. S. Manohar, C. Das, and V. Kakati,* "Bone Tissue Engineering Scaffolds: Materials and Methods," 3D Print Addit Manuf, vol. 11, no. 1, pp. 347–362, Feb. 2024, doi: 10.1089/3dp.2022.0216.

[21] *M. Hussain, S. M. Khan, M. Shafiq, and N. Abbas*, "A review on PLA-based biodegradable materials for biomedical applications," Giant, vol. 18, p. 100261, Jun. 2024, doi: 10.1016/j.giant.2024.100261.

[22] *C. Abeykoon, P. Sri-Amphorn, and A. Fernando*, "Optimization of fused deposition modeling parameters for improved PLA and ABS 3D printed structures," International

Journal of Lightweight Materials and Manufacture, vol. 3, no. 3, pp. 284–297, Sep. 2020, doi: 10.1016/j.ijlmm.2020.03.003.

[23] *I. Buj-Corral, A. Bagheri, A. Domínguez-Fernández, and R. Casado-López, "*Influence of infill and nozzle diameter on porosity of FDM printed parts with rectilinear grid pattern," Procedia Manuf, vol. 41, pp. 288–295, 2019, doi: 10.1016/j.promfg.2019.09.011.

[24] *S. Brischetto and R. Torre,* "Tensile and compressive behavior in the experimental tests for pla specimens produced via fused deposition modelling technique," Journal of Composites Science, vol. 4, no. 3, 2020, doi: 10.3390/jcs4030140.

[25] *B. Pernet, J. K. Nagel, and H. Zhang,* "Compressive Strength Assessment of 3D Printing Infill Patterns," in Procedia CIRP, Elsevier B.V., 2022, pp. 682–687. doi: 10.1016/j.procir.2022.02.114.

[26] *A. Mustakangas, A. Hamada, and A. Järvenpää,* "Enhancement of the Compressive Strength of 3D-Printed Polylactic Acid(PLA) by Controlling Internal Pattern," Materials Science Forum, vol. 1023, pp. 75–81, Mar. 2021, doi: 10.4028/www.scientific.net/MSF.1023.75.

[27] *W. Soud, I. Baqer, and M. Ahmed*, "Experimental Study of 3D printing Density Effect on the Mechanical Properties of the Carbon-Fiber and Polylactic Acid Specimens," Engineering and Technology Journal, vol. 37, no. 4A, pp. 128–132, Apr. 2019, doi: 10.30684/etj.37.4a.3.

[28] *N. S. Hmeidat, B. Brown, X. Jia, N. Vermaak, and B. Compton*, "Effects of infill patterns on the strength and stiffness of 3D printed topologically optimized geometries," Rapid Prototyp J, vol. 27, no. 8, pp. 1467–1479, Sep. 2021, doi: 10.1108/RPJ-11-2019-0290.

[29] *B. Aloyaydi, S. Sivasankaran, and A. Mustafa*, "Investigation of infill-patterns on mechanical response of 3D printed poly-lactic-acid," Polym Test, vol. 87, p. 106557, Jul. 2020, doi: 10.1016/J.POLYMERTESTING.2020.106557.

[30] H. *K. Dave et al.,* "Compressive strength of pla based scaffolds: effect of layer height, infill density and print speed," 2019.

[31] *J. Liu et al.*, "Effect of Infill Parameters on the Compressive Strength of 3D-Printed Nylon-Based Material," Polymers (Basel), vol. 15, no. 2, p. 255, Jan. 2023, doi: 10.3390/polym15020255.

[32] *S. K. Mangla, Y. Kazancoglu, M. D. Sezer, N. Top, and I. Sahin*, "Optimizing fused deposition modelling parameters based on the design for additive manufacturing to enhance product sustainability," Comput Ind, vol. 145, p. 103833, Feb. 2023, doi: 10.1016/j.compind.2022.103833.

[33] *A. H. Foroughi, D. Liu, and M. J. Razavi,* "Simultaneous optimization of stiffness, permeability, and surface area in metallic bone scaffolds," Int J Eng Sci, vol. 193, p. 103961, Dec. 2023, doi: 10.1016/j.ijengsci.2023.103961.

[34] *K. Hayashi, R. Kishida, A. Tsuchiya, and K. Ishikawa*, "Superiority of Triply Periodic Minimal Surface Gyroid Structure to Strut-Based Grid Structure in Both Strength and Bone Regeneration," ACS Appl Mater Interfaces, vol. 15, no. 29, pp. 34570–34577, Jul. 2023, doi: 10.1021/acsami.3c06263.

[35] *E. Maevskaia, J. Guerrero, C. Ghayor, I. Bhattacharya, and F. E. Weber*, "Triply Periodic Minimal Surface-Based Scaffolds for Bone Tissue Engineering: A Mechanical, In Vitro and In Vivo Study," Tissue Eng Part A, vol. 29, no. 19–20, pp. 507–517, Oct. 2023, doi: 10.1089/ten.tea.2023.0033.

[36] *P. A. Khan, A. Raheem, C. Kalirajan, K. G. Prashanth, and G. Manivasagam*, "In Vivo Assessment of a Triple Periodic Minimal Surface Based Biomimmetic Gyroid as an Implant Material in a Rabbit Tibia Model," ACS Materials Au, vol. 4, no. 5, pp. 479–488, Sep. 2024, doi: 10.1021/acsmaterialsau.4c00016.